Ground-Based Millimeter- and Submillimeter-Wave Observations of Low Vapor and Liquid Water Contents

Domenico Cimini, Ed R. Westwater, *Fellow, IEEE*, Albin J. Gasiewski, *Fellow, IEEE*, Marian Klein, *Member, IEEE*, Vladimir Ye Leuski, and James C. Liljegren

***Abstract*—Ground-based observations at millimeter (mm) and submillimeter (submm) wavelengths were collected at the Atmospheric Radiation Measurement Program site at Barrow, AK, during the Arctic winter by a new 25-channel radiometer. A weighting function analysis is presented to demonstrate the enhanced sensitivity of mm- and submm-wave (50–400 GHz) radiometers to low vapor and liquid water contents with respect to conventional instruments such as the ones operating at centimeter (cm) wavelengths (20–30 GHz). In addition, based on measurements, we carried out a quantitative analysis of mm- and submm-wavelength sensitivity, yielding improvement factors from 1.5 to 69 for precipitable water vapor (PWV) and 3 to 4 for liquid water path (LWP) when compared to 20–30 GHz radiometers. Furthermore, using a simulated data set, we evaluate the effect of hydrometeor scattering: Given the conditions occurring during the experiment, the scattering contribution is within the instrumental noise for most, but not all, of the considered channels. With the same data set, we demonstrate that in the dry conditions of the Arctic, a simple linear regression yields satisfactory results when applied on selected mm- and submm-wave channels. For a dual-channel combination, the expected accuracy is ∼0.23 (0.007) mm for PWV (LWP), when using mm- and submm-wavelengths, whereas it is 0.37 (0.012) mm using cm-wave channels. When the retrieval is applied to real observations, the accuracy is found in agreement with theoretical expectations.**

***Index Terms*—Atmospheric measurements, microwave radiometry, remote sensing.**

Manuscript received July 1, 2006; revised November 6, 2006. This work was supported by the Environmental Sciences Division, Department of Energy under the Atmospheric Radiation Measurement Program. The work of D. Cimini was supported by the Cooperative Institute for Research in Environmental Sciences, University of Colorado, and the Institute of Methodologies for Environmental Analysis (IMAA), National Research Council (CNR).

D. Cimini was with the Cooperative Institute for Research in Environmental Sciences, Boulder, CO 80309-0216 USA, and the Institute of Methodologies for Environmental Analysis, Italian National Research Council (IMAA/CNR), 00185, Rome, Italy. He is now with CETEMPS, University of L'Aquila, 67100 Coppito-L'Aquila, Italy.

E. R. Westwater is with the Center for Environmental Technology, Department of Electrical and Computer Engineering, and also with the Cooperative Institute for Research in Environmental Sciences, University of Colorado at Boulder, Boulder, CO 80309-0425 USA.

A. J. Gasiewski is with the Center for Environmental Technology, Department of Electrical and Computer Engineering, University of Colorado at Boulder, Boulder, CO 80309-0425 USA.

M. Klein and V. Y. Leuski are with the Cooperative Institute for Research in Environmental Sciences, University of Colorado at Boulder, Boulder, CO 80309-0425 USA.

J. C. Liljegren is with the Argonne National Laboratory, Argonne, IL 60439 USA.

Digital Object Identifier 10.1109/TGRS.2007.897450

I. Introduction

ACCURATE measurements of the atmospheric water vapor and cloud properties in the Arctic are essential for improving the modeling of the energy budget of the Earth [1]. However, water vapor and cloud liquid measurements during Arctic conditions are difficult because of the lack of sensitivity of conventional instruments to low amounts. In fact, the Arctic region is characterized by extremely dry conditions; during winter, precipitable water vapor (PWV) and liquid water path (LWP) are usually below 5 [2] and 0.2 mm [3], respectively. It follows that the accuracy of existing instrumentation is limiting the development of theory and modeling of the Arctic radiative processes. On the other hand, millimeter (mm) and submillimeter (submm) wavelengths offer a powerful tool to increase the sensitivity during Arctic conditions [2]. Therefore, the Microwave System Development branch of the National Oceanic and Atmospheric Administration (NOAA) Physical Science Division (PSD) designed and developed a 25-channel radiometer that is operating in the mm- and submm-wavelength spectral regions. The instrument, which is named the Ground-based Scanning Radiometer (GSR), was first deployed during the Arctic Winter Radiometric Experiment [4], collecting about one month of observations.

In Section II, details of the GSR and other instruments that are operating during the experiment are given. In Section III, we demonstrate the increased sensitivity of mm- and submm-wavelength channels to small changes in PWV and LWP with respect to conventional microwave instrumentations. In Section IV, we present first results of PWV and LWP retrievals from GSR obtained with a simple linear regression technique, discussing the comparison with operational products. Section V concludes with a summary and plans for future work.

II. Experimental Setup

The Arctic Winter Radiometric Experiment [4] was held at the Atmospheric Radiation Measurement (ARM) Program's North Slope of Alaska (NSA) site near Barrow, AK, from March 9 to April 9, 2004. During this experiment, the recently developed 25-channel GSR was first deployed. This instrument includes five radiometers providing: 12 channels in the low-frequency wing of the 60-GHz oxygen complex (50.2, 50.3, 51.76, 52.625, 53.29, 53.845, 54.4, 54.95, 55.52, 56.025, 56.215, and 56.325 GHz); two channels at 89 GHz

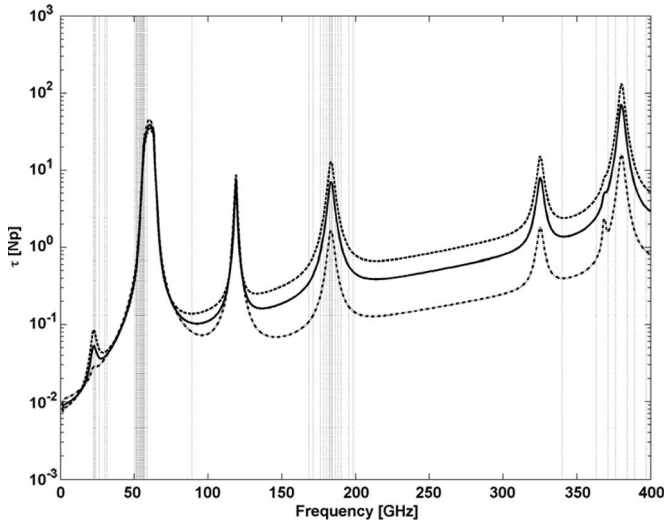

Fig. 1. Atmospheric opacity for standard Arctic conditions with 1, 5, 10 mm PWV (shown with dash-dotted, solid, and dashed lines, respectively). Vertical dotted lines indicate the spectral location of MWR, MWRP, and GSR channels.

[horizontal (H) and vertical (V) polarizations]; seven channels distributed around the 183.31-GHz water vapor absorption line (183.31 ± 0.55, ±1, ±3.05, ±4.7, ±7, ±12, ±16 GHz); two polarized channels at 340 GHz (H and V); and three channels around the 380.2-GHz water vapor line (380.197 ± 4, ±9, ±17 GHz). The channels were selected to provide simultaneous retrievals of PWV, LWP, and low-resolution temperature and humidity profiles. The core of the instrument, which is called the scanhead, is able to scan continuously in elevation. During the experiment, it scanned from 20° to 160°, dwelling at 1.0, 1.5, 2.0, 2.5, 3.0, and 3.5 air masses both sides in 2-min cycles. In this paper, we show only observations collected at zenith, although data at other angles are involved in the calibration process by using the so-called tipping curve method [5]. The calibration procedure includes frequent (∼150 ms) switching between internal loads for monitoring the receiver stability and less frequent observations of two external targets (located in a protected environment) to perform a complete end-to-end calibration every 2 min. Moreover, the tipping curve method is applied to refine calibration of channels with low attenuation. The expected absolute accuracy is on the order of 1–2 K, depending upon channel [5].

During the experiment, the GSR joined the resident instrumentation at the ARM NSA site, including a dual-channel microwave radiometer (MWR) and a 12-channel MWR profiler (MWRP). The MWR has two channels near the weak 22.235-GHz water vapor line (23.8 and 31.4 GHz), whereas the MWRP has five channels in the same region (22.235, 23.035, 23.835, 26.235, and 30.0 GHz), seven channels along the wing of the 60-GHz oxygen complex (51.25, 52.28, 53.85, 54.94, 56.66, 57.29, and 58.8 GHz), plus an infrared channel at 10 μm. The spectral locations of GSR, MWR, and MWRP channels are shown in Fig. 1, together with clear-sky atmospheric opacity τ spectra corresponding to standard Arctic atmosphere with 1, 5, and 10 mm of PWV. This figure is further discussed in Section III.

III. Sensitivity Study

As illustrated in Fig. 1 (see also [6]), the atmospheric opacity in the 1–400-GHz range shows an increase with frequency, due to the absorption of the water vapor continuum, and peaks due to resonant absorption lines of oxygen (50–60, 118.75, and 368.49 GHz) and water vapor (22.235, 183.31, 325.15, and 380.20 GHz). In particular, the absorption at 183.31- and 380.20-GHz lines is one to three orders of magnitude larger than that at 22.235 GHz. Moreover, when the water vapor profile is scaled to result in PWV from 1 to 10 mm, higher frequencies show significantly larger variations with respect to the 20–30-GHz range. Additionally, the frequency-squared dependence of liquid water absorption (not shown) causes the opacity due to liquid clouds to be larger for mm and submm channels than for lower frequency channels. These features translate into enhanced sensitivity of mm and submm wave to low amounts of PWV and LWP, which makes them appealing for deployment in very dry environments, such as polar regions or elevated sites. Note that in moderate to humid environments, most mm and submm channels would gradually saturate (depending on PWV and frequency), and thus become more sensitive to temperature than humidity. Thus, the enhanced sensitivity of mm and submm radiometry comes at the expense of a higher degree of nonlinearity with respect to conventional frequencies (20–30 GHz). Quantitative discussions are given in Section III-A and B.

A. Weighting Function Analysis

A weighting function analysis provides quantitative support to our previous supposition. The incremental weighting functions [7] give an estimate of the sensitivity of a particular channel to changes of a given atmospheric variable (e.g., temperature, water vapor density, and liquid water content) and thus indicate the ability to retrieve that particular parameter from passive observations. In Fig. 2, we show weighting function profiles for selected MWR, MWRP, and GSR channels as computed using the Arctic atmospheres introduced before (PWV = 1, 5, 10 mm). In particular, Fig. 2(a) shows the water vapor weighting function WF_ρ for the two MWR channels at 23.8 and 31.4 GHz, the MWRP channel at 22.235 GHz, and the GSR channel at 89 GHz. Note that the MWRP channel is located at the center of the water vapor line, thus corresponding to the maximum absorption in the 20–30 GHz range, whereas 89 GHz corresponds to the lowest absorption among the GSR channels. WF_ρ at 23.8 and 31.4 GHz show little variation with height, which makes these two channels optimal for estimates of integrated contents. Conversely, WF_ρ at 22.235 and 89 GHz show vertical structure with inverse trends. In any case, these four channels exhibit sensitivity to water vapor of the same order of magnitude, with almost no dependence on water vapor content. This feature is kept for higher PWV contents (not shown), which makes low-frequency channels eligible for water vapor observations in any environmental conditions. However, considering the instrumental error, the sensitivity shown in Fig. 2(a) is not enough to capture very small variations in PWV. As a comparison, Fig. 2(b) shows WF_ρ for

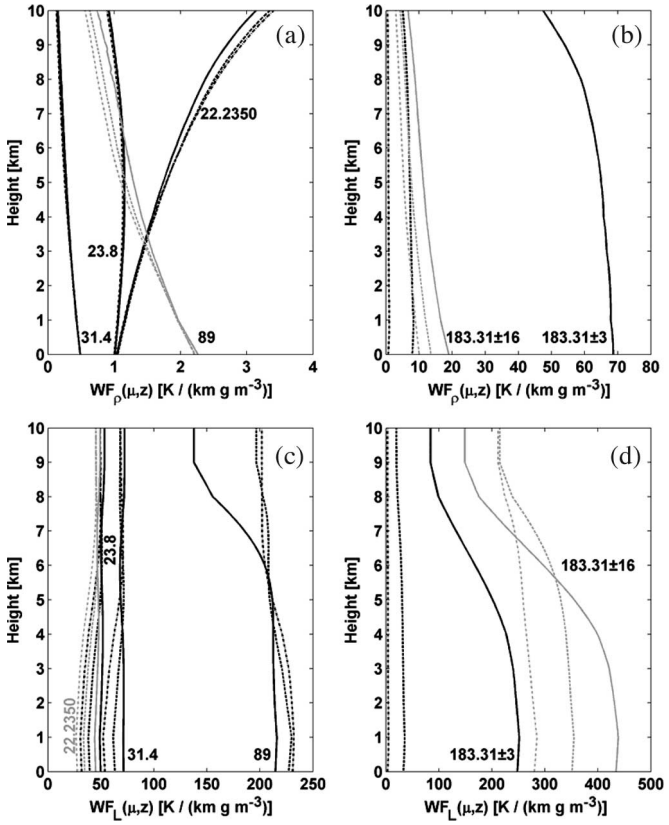

Fig. 2. (a)–(b) Water vapor and (c)–(d) liquid water weighting functions WF as a function of height z for selected MWRP and GSR channels. WFs were computed with a standard Arctic atmosphere, setting PWV to 1, 5, and 10 mm (shown with solid, dotted, and dashed lines, respectively). Zenith observations are considered in this plot (air mass $\mu = 1$).

GSR 183.31 $\pm$ 3.05 and $\pm$16 GHz channels. For PWV $=$ 1 mm, these channels show WF$_\rho$ 10 to 60 times larger than the ones in Fig. 2(a), leading to enhanced sensitivity to small variations in water vapor. However, the sensitivity is greatly reduced when PWV increases to 5 or 10 mm. This is particularly true for opaque channels near the center of absorption lines, e.g., 183.31 $\pm$ 3.05 GHz. This channel has almost no sensitivity (i.e., saturates) to PWV equal or larger than 10 mm. Conversely, channels away from the line center (e.g., 183.31 $\pm$ 16 GHz) still show five to ten times larger sensitivity than conventional 20–30-GHz channels. Therefore, it follows that a proper mm and submm channel combination, spanning from moderate to high absorption, would provide high sensitivity for all the conditions typical of the Arctic. This is obtained in the GSR system with ten channels, ranging from the wings to the near-center of two strong water vapor lines.

Similar considerations apply for the liquid water weighting functions WF$_L$ in Fig. 2(c) and (d). In particular, we notice significant larger values for WF$_L$ at 89 and 183.31 $\pm$ 16 GHz with respect to lower frequency channels. In addition, the percent change attributable to water vapor is as large as for 20–30-GHz channels. On the other hand, 183.31 $\pm$ 3.05 GHz shows large WF$_L$ for low PWV content but saturates very quickly with increasing PWV. Of course, this channel will only be used for the retrieval of very low PWV.

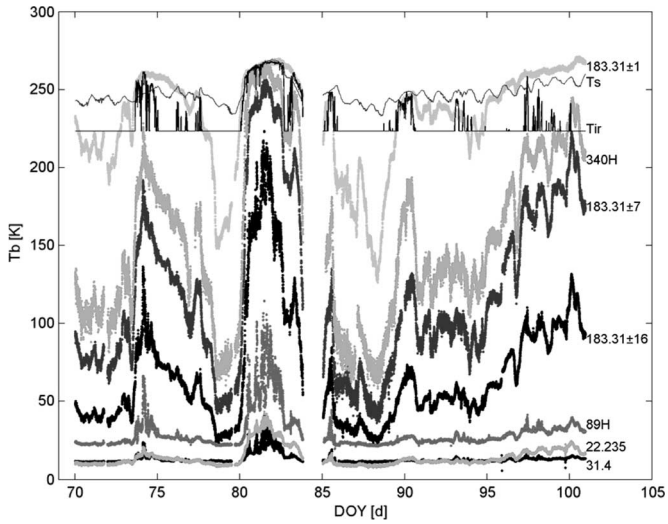

Fig. 3. Time series of T_s, $T_{\rm ir}$, and T_b's at selected MWR, MWRP, and GSR channels during the whole Arctic Winter Radiometric Experiment. Note that the lowest value read by the MWRP infrared sensor ($T_{\rm ir}$) was fixed by the manufacturer to 223.2 K. Time is expressed in day of the year.

B. Brightness Temperature Sensitivity

As an example of the observations collected during the experiment, Fig. 3 illustrates a one-month time series of surface temperature T_s, sky infrared temperature $T_{\rm ir}$, and brightness temperature T_b at selected MWR, MWRP, and GSR channels. Note that $T_{\rm ir}$ varies between T_s and 223.2 K. The latter value was set by the manufacturer as the lowest temperature read by the infrared sensor. This threshold can be used to derive a simplistic cloud detection algorithm; every time $T_{\rm ir} > 223.2$ K, a cloud is detected. Conversely, $T_{\rm ir} = 223.2$ K corresponds to clear-sky (this may not detect high cirrus, but its effect on microwave is considered negligible for now). Reading the figure from bottom to top, we note the following.

Both 22.235 and 31.4 show low T_b, with very little variation in clear skies ($T_{\rm ir} = 223.2$ K). Quite surprising, T_b at 22.235 GHz is sometimes lower than at 31.4 GHz, indicating that the atmosphere is so dry that the oxygen continuum is dominating over the water vapor absorption.

The 89 GHz T_b shows clear-sky fluctuations similar to 22.235 GHz T_b, although it is some 10 K warmer. However, in the presence of clouds, as from 80 to 84 days of the year (DOY), 89 GHz shows larger dynamic range, as expected, considering the frequency-squared dependence of liquid water absorption.

Channels around the 183.31-GHz line (we only show 183.31 $\pm$ 16, $\pm$7, and $\pm$1 as representatives of relatively weak, moderate, and strong absorptions) show much more pronounced clear-sky fluctuations. In particular, it is interesting to see that during dry periods (87–89 DOY) the 183.31 $\pm$ 1 GHz T_b shows the largest response, whereas during humid conditions (95–97 DOY) this channel is almost completely saturated and resembles the surface temperature T_s. However, in the same humid period, 183.31 $\pm$ 16 and $\pm$7 GHz channels are still very responsive. Even in the case of thick low clouds (as indicated by periods with $T_{\rm ir}$ coincident with T_s, e.g., 80–84 DOY), 183.31 $\pm$ 16 GHz channel is very responsive, demonstrating characteristics typical of a window channel.

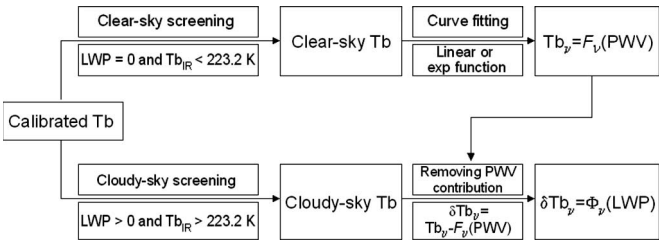

Fig. 4. Flowchart of the algorithm used to estimate the channel sensitivity to PWV and LWP. F_ν and Ω_ν are functions of PWV and LWP determined by functional fit for each channel (i.e., frequency) and represent the continuous curves in Figs. 5 and 6.

The 340-GHz channel behaves similarly to 183.31 $\pm$ 16 GHz during clear-sky observations, although it shows enhanced response to liquid clouds, as expected due to its higher frequency. Note also that this channel shows larger noise with respect to the other GSR channels, due to some calibration difficulties described in [5].

1) T_b Sensitivity to PWV: To give an experimental quantitative estimate of the sensitivity of centimeter- (cm), mm- and submm-wave channels to changes in PWV and LWP, we have processed the data collected by MWR, MWRP, and GSR following the scheme pictured in Fig. 4. The calibrated brightness temperatures were first divided into clear and cloudy conditions, as indicated in Fig. 4, according to the ARM operational LWP retrieval (based on MWR observations) and the sky infrared temperature measured by the MWRP 10-μm channel. Once clear-sky T_b's have been selected, the relationship with PWV (ARM operational retrieval) is estimated by curve fitting. Assuming the following relationship (see the Appendix):

$$B_\nu(T_b) = B_\nu(T_c) \cdot e^{-\tau} + B_\nu(T_{\mathrm{mr}}) \cdot (1 - e^{-\tau}) \qquad (1)$$

where $\tau = \tau_d + k_V V$ and V indicates PWV, we compute a three-parameter fit ($[\tau_d, k_V, B(T_{\mathrm{mr}})]$) using the unconstrained nonlinear optimization (Nelder–Mead simplex method [8]). The corresponding T_b is then obtained by inverting the Planck function B_ν. Setting the initial value to $[0, 1, B(\max(T_b))]$ usually leads to a convergence for all channels but the most transparent ones (i.e., 20–90 GHz). Nonetheless, for these channels the opacity is low enough to use the following equation (see the Appendix):

$$T_b = I + S \cdot V \qquad (2)$$

so we adopt a two-parameter fit ($[I, S]$) solving with the least-squares method.

Following the above method, for each channel we fitted the observed T_b with a line, resulting in the curves shown in Fig. 5. The above suppositions about channel sensitivity become evident in this plot. In fact, the sensitivity of each channel to change in PWV is given by the slope of the fit (i.e., dT_b/d PWV) at any value of PWV. Thus, channels with a relatively flat fit (as 22.235, 30, and 90 GHz) show little sensitivity to small PWV changes. Moreover, the slopes remain nearly constant throughout the available range, indicating that these channels offer the same sensitivity regardless of the PWV

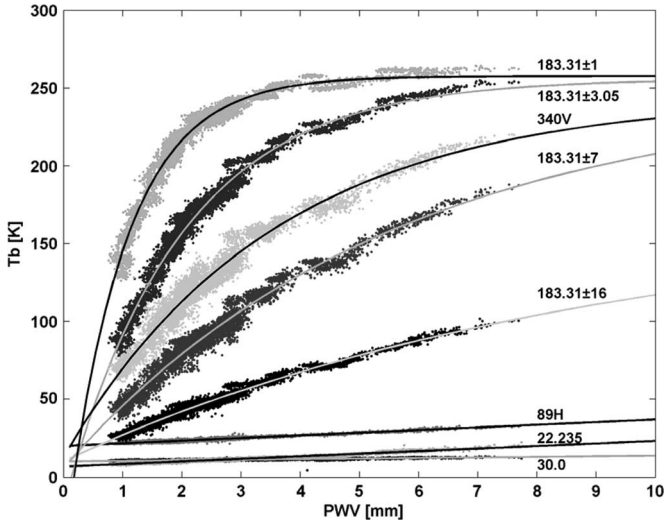

Fig. 5. Measured brightness temperature response to PWV in clear sky for selected MWRP and GSR channels. Lines through the observed data represent two- and three-parameter fit, as described in Section III-B1.

absolute value. Similar considerations apply to 183.31 $\pm$ 7 and $\pm$16 GHz channels, although here the sensitivity (i.e., slope) is much larger. As already mentioned, the curves corresponding to 22.235 and 30.0 GHz cross each other, as the oxygen contribution starts to dominate over the water vapor absorption at very low PWV. Conversely, more opaque channels show nonlinear relationship with PWV; the slope is very steep (i.e., high sensitivity) in a reduced range, but then the curve bends and the slope tends to zero (i.e., saturation). This is the case for 183.31 $\pm$ 1 and $\pm$3 GHz channels, for which the sensitivity is not uniquely determined, but it is rather a function of PWV.

Nonetheless, limiting the range of PWV to less than 1.5 mm and assuming the linear relationship in (2) for all the channels, we can give a single estimate to compare with the simulations found in [2] that were obtained using the absorption model of [9] and [10]. Results are shown in Table I for all MWR, MWRP, and GSR channels. While a comparison between different absorption models is beyond the scope of this paper, in Table I we add the results obtained using the model in [11] not only to cover all the available channels but also to give an idea of the uncertainty in sensitivity associated with models. Simulations are computed from a historical database (HDB) of 292 radiosondes launched in wintertime at the ARM NSA. The radiosonde thermodynamic profiles have been associated with a set of realistic profiles of liquid and ice water contents [12] covering the conditions experienced during the experiment, in terms of LWP and ice water path (IWP). Thus, we generated a set of 559 clear and cloudy profiles (called hereafter ARM NSA HDB) that we run through a radiative transfer model [12] to produce the corresponding synthetic brightness temperatures.

From Table I, we see that our experimental estimates usually fit within the 99% confidence interval the corresponding values predicted with models, although this is not always the case. Nevertheless, Table I demonstrates that the sensitivity of mm and submm channels to very low PWV outperforms the one at 20–30 GHz by a factor ranging from 1.5 to 69.

TABLE I
SENSITIVITY OF MWR, MWRP, AND GSR CHANNELS TO LOW PWV AMOUNTS

	WVIOP2004 (measured)	ARM NSA HDB (simulations)	After [2] (simulations)
	0.8<PWV<1.5 mm	0.8<PWV<1.5 mm	0.5<PWV<1.5 mm
f (GHz)	S ± 99%CI (K/mm)	S ± 99%CI (K/mm)	S (K/mm)
23.8	1.27 ± 0.05	1.34 ± 0.01	1.25
31.4	0.28 ± 0.07	0.43 ± 0.01	0.34
22.235	1.63 ± 0.16	1.72 ± 0.05	
23.035	1.46 ± 0.14	1.61 ± 0.01	
23.835	1.22 ± 0.14	1.33 ± 0.01	
26.235	0.60 ± 0.15	0.72 ± 0.01	
30.0	0.36 ± 0.14	0.46 ± 0.01	
89 V	1.72 ± 0.17	2.10 ± 0.03	1.81
89 H	1.75 ± 0.19		
183.31±16	14.13 ± 0.77	19.48 ± 2.53	
183.31±12	17.47 ± 0.93	23.91 ± 2.48	
183.31±7	30.85 ± 2.06	39.02 ± 3.46	39.20
183.31±4.7	52.06 ± 2.39	55.39 ± 3.26	
183.31±3.05	70.66 ± 3.17	69.45 ± 2.68	75.00
183.31±1	88.63 ± 4.01	82.77 ± 4.67	78.60
183.31±0.55	88.66 ± 4.33	79.66 ± 5.29	
340 V	40.51 ± 2.76	47.13 ± 4.72	44.50
340 H	33.76 ± 3.07		
380.197±4	31.27 ± 1.77	23.63 ± 6.64	
380.197±9	80.21 ± 3.59	71.06 ± 6.59	
380.197±17	68.52 ± 3.44	69.19 ± 5.02	

2) T_b Sensitivity to LWP: The next step of the procedure illustrated in Fig. 4 is to quantify the channel sensitivity to LWP. Thus, we select cloudy-sky T_b's according to ARM operational LWP and MWRP $T_{\rm ir}$, and we remove the PWV contribution computed using the ARM operational PWV retrievals and the T_b–PWV relationship we have determined in the previous step (see Fig. 4). The remaining δT_b is assumed to be the contribution of liquid water emission (neglecting scattering, see Section IV) and is thus fitted against LWP with a linear curve. Results for selected channels are shown in Fig. 6; slopes and intercepts for the set of channels exhibiting relatively low water vapor absorption, i.e., window channels, are also reported in Table II, together with simulation results based on ARM NSA HDB.

From Fig. 6, it is evident that 89 and 183.31 ± 16 GHz channels present steeper slopes (i.e., larger sensitivity to LWP) with respect to 20–30 GHz, by a factor of 3 to 4. Note that the intercept, which should be zero if the dry air and water vapor contributions have been removed effectively, is usually small, particularly for 22–31-GHz channels (< 0.4 K). For higher frequency channels, the intercept is larger (1–3 K), probably due to a combination of the larger sensitivity to small LWP uncertainties (inherent in the MWR retrieval) and larger errors associated with the absolute calibration. Nonetheless, the intercept still remains modest if compared to the corresponding range of variation due to PWV changes.

As seen in Tables I and II, we obtain significantly different results for the two polarized channels at 340 GHz. Since during the experiment the 340-GHz radiometer experienced excessive noise resulting in additional uncertainty, we warn that results for 340-GHz channels should be taken with care. Assuming the models as a reference, we may say that the V polarization channel gives more reliable results.

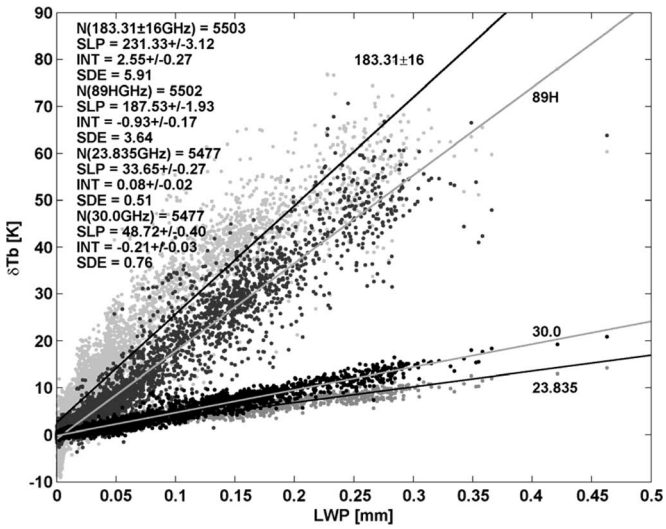

Fig. 6. Measured brightness temperature response to LWP for selected MWRP and GSR channels. The contribution of water vapor has been removed following the diagram in Fig. 4. Number of elements (N), slope (SLP), and intercept (INT) of a linear fit, and standard estimation error (SDE) for all four channels are also reported in the figure. SLP is in Kelvin per millimeter, whereas INT and SDE are in Kelvin. Uncertainties represent the 99% confidence interval.

TABLE II
SENSITIVITY OF WINDOW CHANNELS TO LOW LWP AMOUNTS

	WVIOP2004 (measured)		ARM NSA HDB (simulations)	
	0.0<LWP<0.5 mm		0.0<LWP<0.5 mm	
f (GHz)	S ± 99%CI (K/mm)	I ± 99% CI (K)	S ± 99%CI (K/mm)	I ± 99% CI (K)
23.8	32.28 ± 0.08	0.14 ± 0.01	35.50 ± 0.69	0.09 ± 0.09
31.4	55.61 ± 0.08	0.14 ± 0.01	57.00 ± 0.79	0.15 ± 0.10
22.235	28.34 ± 0.32	0.34 ± 0.03	32.53 ± 1.58	-0.13 ± 0.20
23.035	32.79 ± 0.30	0.27 ± 0.03	33.48 ± 0.68	0.05 ± 0.09
23.835	33.65 ± 0.27	0.08 ± 0.02	35.60 ± 0.69	0.09 ± 0.09
26.235	39.85 ± 0.35	-0.11 ± 0.03	42.47 ± 0.74	0.12 ± 0.09
30.0	48.72 ± 0.40	-0.21 ± 0.03	53.10 ± 0.78	0.14 ± 0.10
89 V	187.89 ± 1.92	-0.82 ± 0.16	191.84 ± 2.25	1.01 ± 0.29
89 H	187.53 ± 1.93	-0.93 ± 0.17		
183.31±16	231.33 ± 3.12	2.55 ± 0.27	233.67 ± 9.53	3.76 ± 1.21
183.31±12	195.61 ± 3.25	2.89 ± 0.28	204.37 ± 10.20	3.69 ± 1.30
340 V	108.71 ± 5.25	3.74 ± 0.45	104.01 ± 14.41	5.10 ± 1.83
340 H	141.10 ± 5.99	6.86 ± 0.52		

Finally, the values reported in Tables I and II demonstrate the enhanced sensitivity of mm and submm channels with respect to conventional radiometry for measurements of low PWV and

LWP contents. It is worth stressing that these conclusions are valid just for very dry conditions, as the sensitivity of mm and submm channels would fade with increasing PWV. On the contrary, the sensitivity of 20–30-GHz channels remains almost invariant, making these frequencies usable under a larger range of conditions.

IV. Evaluation of Scattering Contribution

When moving from cm-wave to shorter wavelengths, a larger contribution by hydrometeor scattering is expected. The total effect of hydrometeor scattering on the measured T_b depends on many factors, including size ratio (i.e., wavelength to drop size), particle shape and phase, water vapor content, and the temperature contrast between the observation direction and the surroundings. A detailed study on each factor is beyond our goal, although we are interested in understanding what is the magnitude we should expect for the total effect.

To study the scattering contribution, we processed the ARM NSA HDB with the Discrete Ordinate Tangent Linear Radiative Transfer model (DOTLRT), which relies on a multiple-stream algorithm for calculating the radiative transfer and the Jacobian under arbitrary scattering and absorbing conditions [13]. In the DOTLRT model, we assumed the cloud microphysics described in [14], consisting of five types of spherical hydrometeors (liquid, ice, rain, snow, and graupel) with particle size distribution parameterized as a function of the intrinsic density and the total hydrometeor content. The dielectric constant for homogeneous liquid and ice particles is obtained from the Debye relaxation formulas, whereas heterogeneous hydrometeors are treated with a dielectric mixing theory.

Since the DOTLRT model allows the user to enable/disable the scattering calculation, we performed two independent runs for the ARM NSA HDB: one with scattering activated and one without; the T_b difference between the two runs indicates the contribution due to scattering. Results for most representative channels are shown in Figs. 7 and 8 for pure liquid and pure ice clouds, respectively, which represent two extreme cases. The two MWR channels have been selected as representatives of the cm-wave range, whereas the other channels in Figs. 7 and 8 correspond to the most transparent channel of each GSR radiometer. These are associated with the maximum scattering contribution because of the largest T_b contrast between the sky and the surroundings. Other channels in the same band would show smaller scattering contribution. The following considerations apply similarly to the cases of pure liquid and ice clouds (Figs. 7 and 8). As expected, channels in the cm-wave range have negligible scattering contribution, with differences within 0.01 K. The contribution is larger at 89 GHz, although it remains within 0.1 K and thus can still be considered negligible. At 183.31 $\pm$ 16 GHz, the scattering contribution increases fairly linearly with LWP and IWP, until it reaches a sort of plateau, likely due to the reduced T_b contrast. However, in the considered range the contribution remains lower than 0.6 K, which is within the total uncertainty of this channel [5]. As we anticipated, this applies to other channels in the same band. For example, the maximum value is reduced to 0.4 K at 183.31 $\pm$ 7 GHz and 0.1 K at 183.31 $\pm$ 1 GHz. For higher frequency

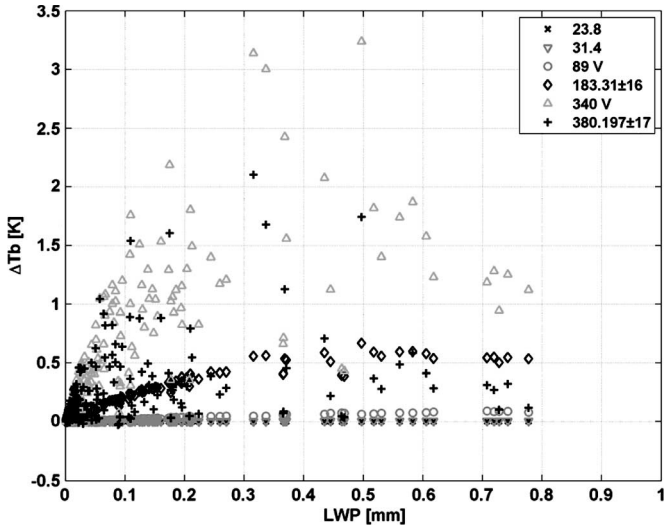

Fig. 7. Evaluation of the scattering contribution using simulated data. Case of pure liquid clouds. ΔT_b results from the difference between T_b computed with and without scattering.

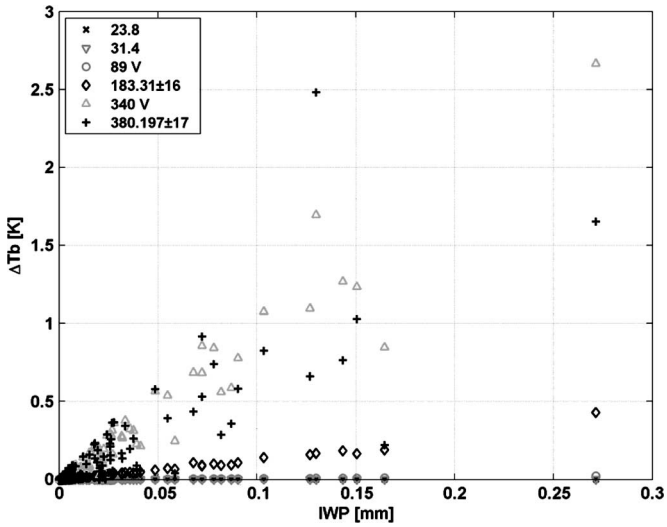

Fig. 8. Evaluation of the scattering contribution using simulated data. Case of pure ice clouds. ΔT_b results from the difference between T_b computed with and without scattering.

channels, the scattering contribution becomes significant. We see that for both 340 GHz and 380.20 $\pm$ 17 the T_b difference increases rapidly with LWP and IWP, reaching up to 3.5 K. For high LWP, the difference tends to decrease, because the absorption dominates over the scattering for liquid water, and the channels become saturated. Conversely, for pure ice clouds, the scattering contribution increase steadily with IWP, and the differences can reach 5 K for IWP larger than 0.3 mm. For other 380.20 channels, the maximum value is limited to 0.5 K at 380.20 $\pm$ 9 GHz and 0.1 K at 380.20 $\pm$ 4 GHz.

It is important to note that the considerations above are strictly valid for the range of LWP and IWP under study. For a broader analysis, conditions typical of other Arctic seasons should be evaluated. Also, results may change if a different microphysics is assumed in DOTLRT, as for example size distribution and/or particle shape. Characteristics typical of the Arctic winter, as reported in [3], are under study.

TABLE III
EXPECTED ACCURACY FOR LINEAR REGRESSION APPLIED TO A VARIETY OF CHANNEL COMBINATIONS. SIMULATED DATA COMPUTED FROM ARM NSA HDB WERE USED

CHANNEL COMBINATION	PWV (mm)	LWP (mm)
MWR	0.37	0.0127
MWRP	0.29	0.0118
GSR(183±1-3-7)	0.93	0.1049
GSR(183±1-3-7-16)	0.83	0.0876
GSR(183±7-16)	0.26	0.0090
GSR(89,183±7)	0.23	0.0071
GSR(89,183±12)	0.28	0.0075
GSR(89,183±16)	0.28	0.0071
GSR(89,183±7-12-16)	0.25	0.0064
GSR(89,183±12-16)	0.23	0.0060
GSR(89,183±7-12)	0.22	0.0066
GSR(89,183±7-16)	0.33	0.0078
GSR(89,183±1-3-7)	0.23	0.0047

V. INITIAL RESULTS FOR RETRIEVALS

Due to the nonlinear response of some of the GSR channels to atmospheric water vapor and liquid water, an appropriate retrieval technique that fully exploits the potential of such measurements should be nonlinear, as done in [15] using four 183-GHz channels. In fact, an optimal estimation method (OEM) [16] that is initialized with a first guess from a numerical weather prediction model, which is also called 1-D Variational Assimilation Retrieval (1D-VAR) [17], [18], is currently being implemented. Nonetheless, looking at Fig. 5, it seems that a linear technique can be applied to the most transparent channels (e.g., 89, 183 $\pm$ 7, 183 $\pm$ 12, 183 $\pm$ 16) with acceptable results.

A simulation study was carried out using a simple linear regression. In an attempt to linearize the problem, we apply the regression to the opacity τ, which is estimated from T_b using the inverse of (1). This step requires a fairly accurate knowledge of $T_{\rm mr}$, particularly for rather opaque channels, since the error associated with the mapping of T_b into τ is in first approximation proportional to the error in $T_{\rm mr}$ divided by the difference between $T_{\rm mr}$ and T_b. In this regard, we recognize that cm-wave channels are advantageous because they are more robust to the uncertainty associated with $T_{\rm mr}$.

The regression was trained with a synthetic *a priori* data set generated from the ARM NSA HDB, which was processed with the absorption model described in [11]. The instrumental error was accounted for by adding normal-distributed random noise to the simulated T_b; a noise level of 0.3 K was assumed for cm-wave channels and 1.0 K for mm- and submm-wave channels. We also add 1.5 K noise to the simulated $T_{\rm mr}$ at all channels, as this is the uncertainty provided by ground-based estimates based on MWRP [5], which will be used in the retrievals. Using an independent set of 63 profiles, we estimated the retrieval accuracy for a variety of channel combinations, as shown in Table III. In particular, the first two combinations correspond to the MWR and MWRP channels, all located in the cm-wave range (22.235–31.4 GHz). The retrieval accuracy obtainable with these channels is on the order of 0.4 mm for PWV and 0.02 mm for LWP. The associated percentage error is considered acceptable for applications in moderate to humid environments and in the presence of heavy clouds, but it becomes large in drier environments and for clouds bearing little water. For example, in the conditions typical of the Arctic, the numbers above may easily lead to percentage errors exceeding 30% or more.

Due to the increased sensitivity shown in the previous section, it is foreseen that retrievals based on mm- and submm-wave channels will improve the accuracy for both PWV and LWP. However, Table III indicates that a linear technique will give unacceptable results when used with opaque channels in their nonlinear regime, as one would expect. This is the case of the 183 $\pm$ 1–3–7 combination. Note that by adding a transparent channel to the set, as in the 183 $\pm$ 1–3–7–16 combination, the retrieval accuracy improves. On the other hand, Table III confirms that linear regression could provide good results when used with a combination of transparent GSR channels (as 89, 183 $\pm$ 7, 183 $\pm$ 12, and 183 $\pm$ 16 GHz) provided that the conditions are dry as in the Arctic.

As already mentioned, a combination of cm- and mm-wave channels, integrated in an OEM framework, would guarantee enough sensitivity in every condition. However, as a first application to real data, we applied the regression coefficients computed from the simulated training set to the GSR observations. In particular, we limit our analysis to a two-channel combination as we want to compare with the ARM operational retrieval based on the dual channel MWR. We choose the 89 and 183 $\pm$ 7 GHz channels for the following reasons: being the most transparent GSR window channel, 89 GHz presents linear behavior and little response to water vapor, resulting in a good LWP channel; on the contrary, 183 $\pm$ 7 GHz is a strong PWV channel, though still showing a fairly linear response.

As discussed in [5], the two polarizations of the GSR 89-GHz radiometer agree well with each other (bias < 0.1 K), although both show a consistent bias with respect to forward model calculations. At this point, this issue is still under study, as there is a lack of evidence whether this bias is due to instrumental or rather modeling error. Since the linear regression is trained with simulated data, this T_b bias would fold into the retrievals; thus, awaiting further study, in this analysis we decide to remove this bias, by simply subtracting 3.5 K from 89 GHz T_b. The retrievals shown herewith are computed using the 89-GHz V polarization.

In Fig. 9, we compare the PWV and LWP retrievals by MWR (ARM operational) and GSR (89, 183 $\pm$ 7 GHz) for the entire set of observations collected during the experiment. Overall, we see a fairly good agreement, with 0.4 and 0.01 mm mean difference for PWV and LWP, respectively. The slope of the linear fit is smaller than 1 for both PWV and LWP, which means that for high vapor or liquid contents the GSR (89, 183 $\pm$ 7 GHz) tends to underestimate with respect to the MWR. This may be a residual effect of the nonlinearity associated with higher frequency channels. Other than this, the comparison is rather satisfactory, and it demonstrates the feasibility of PWV and LWP retrievals using linear regression applied to selected GSR channels. As a further comparison, in Fig. 10 we show two-day time series of MWR and GSR (89, 183 $\pm$ 7 GHz) retrievals. Also illustrated is PWV computed integrating the water vapor profiles measured by radiosondes launched at two sites, one located near the radiometers and the

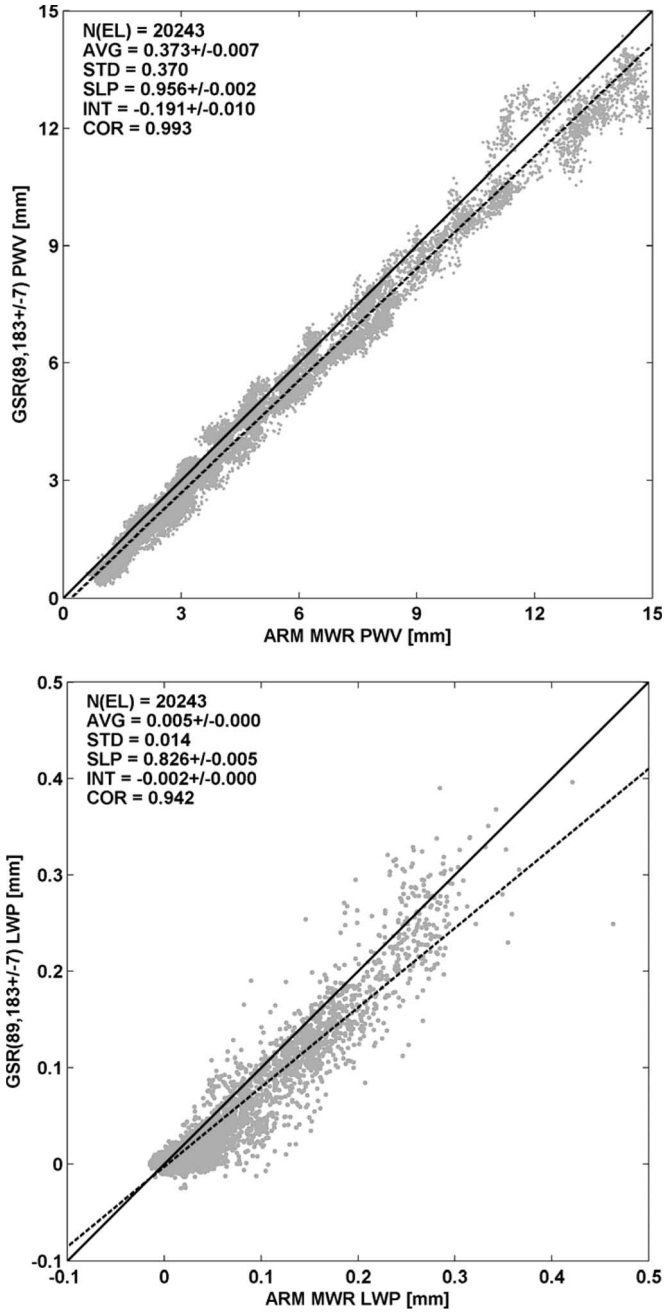

Fig. 9. Comparison of (top) PWV and (bottom) LWP retrievals from MWR and GSR, based on two-channel linear regression (23.8–31.4 GHz for MWR and 89–183.2 $\pm$ 7 for GSR). Number of elements (N), mean X–Y difference (AVG), standard deviation (STD), slope (SLP), and intercept (INT) of linear fit, and correlation coefficients (COR) are also reported. Uncertainties represent the 99% confidence interval, zero meaning uncertainty are smaller than the digits shown.

other 2.4 km away (referred to as GW and DPX, respectively). The radiosondes launched at these two sites have been analyzed in detail [19] and were judged to produce unbiased PWV. It is evident from Fig. 10 that when the MWR PWV departs from GSR PWV, the radiosondes tend to agree with the latter.

Since the launched radiosondes did not carry liquid water sensors, we do not have an independent validation for LWP. Nevertheless, considering the simple cloud detection algorithm based on MWRP $T_{\rm ir}$, a flag is raised every time $T_{\rm ir} > 223.2$ K, although this does not necessarily mean that there is liquid

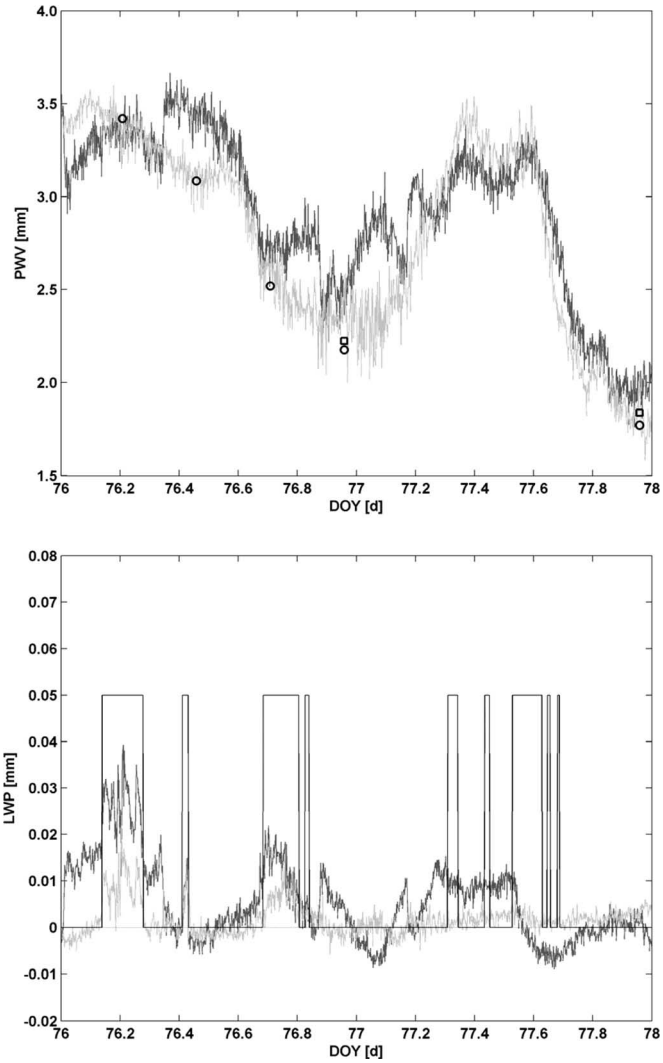

Fig. 10. Time series of (top) PWV and (bottom) LWP as retrieved from (dark gray) MWR and (light gray) GSR (89, 183.2 $\pm$ 7). Black circles and squares represent PWV measured by DPX and GW sondes, respectively. The black solid line represents cloud detection by the MWRP infrared sensor; 0 means clear sky, whereas 0.05 indicates clouds overhead.

water within the cloud. Conversely, when clear sky is detected ($T_{\rm ir} \leq 223.2$ K), it is likely that no liquid water is present overhead.

Therefore, Fig. 10 shows that the ARM and GSR LWP retrieval usually follow each other and correctly detects cloud liquid when the infrared indicates cloud overpass. However, there are evident cases (as in 76.0–76.1 or 76.3–76.4 DOY) in which the ARM operational LWP retrieval gives presence of liquid water where the GSR and the infrared sensors detect none. Although these cases last for a few hours, the associated LWP is pretty small (approaching the uncertainty of MWR) and thus may be related to slight MWR calibration drifts. Because the sensitivity of cm-wave channels to low amounts of LWP is low, even a slight calibration drift can be confused by the retrieval algorithm as an atmospheric feature. On the other hand, these results confirm the impression that the enhanced sensitivity of mm and submm wavelengths would help in these situations and significantly improve the retrieval of low amounts of LWP. Similar considerations apply for another

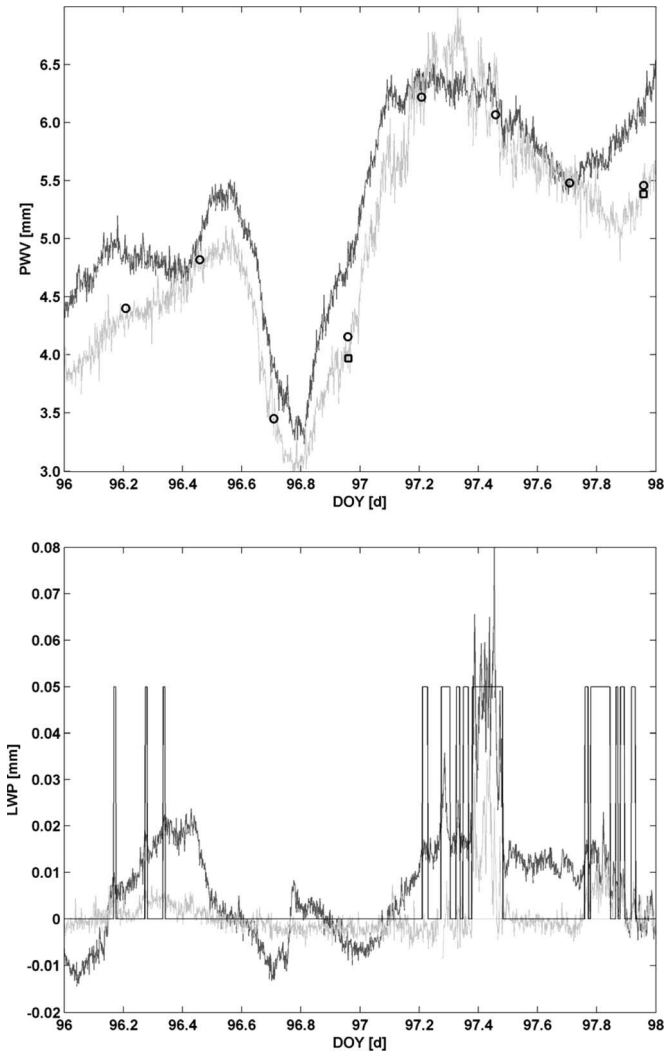

Fig. 11. As in Fig. 10, another example of PWV and LWP retrievals from MWR and GSR (89, 183.2 ± 7).

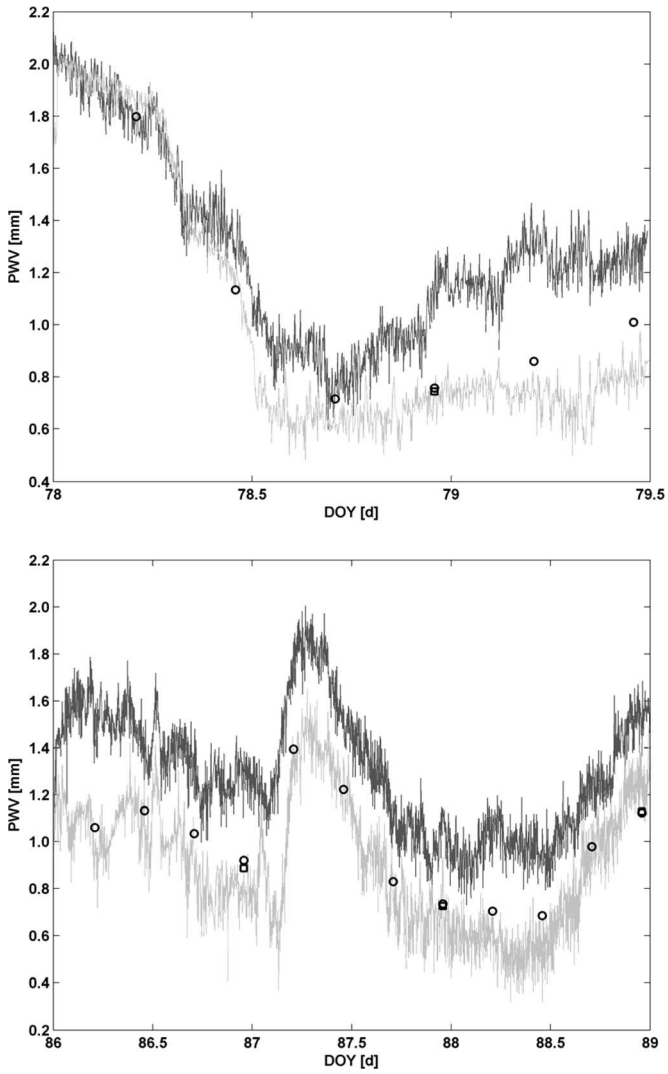

Fig. 12. PWV time series during very dry conditions. PWV from MWR is shown in dark gray, whereas PWV from GSR (89, 183.2 ± 7) is shown in light gray. Black circles and squares represent PWV measured by DPX and GW sondes, respectively.

two-day time series shown in Fig. 11. For both PWV and LWP, it is evident that the GSR retrievals capture the trend described by radiosondes and infrared cloud detection, whereas this is not always the case for MWR. In particular, relatively large departures from the radiosonde PWV and the zero-liquid flag occur.

However, the real strength of mm- and submm-wave channels is when the PWV gets extremely low. Two examples are given in Fig. 12, which are selected from the driest periods encountered during the experiment (PWV as low as 0.6 mm). Here, errors in PWV with respect to radiosondes can reach 50% for MWR retrievals, whereas they remain within 15% for GSR (89, 183 ± 7 GHz).

Extending the comparison to the whole experiment, PWV retrievals from both MWR and GSR (89, 183 ± 7 GHz) agree well with radiosondes, as shown in Fig. 13. The overall scatter is comparable for the two retrievals (∼0.27 mm), although for MWR it is more pronounced at lower values, whereas for GSR (89, 183 ± 7 GHz) it is near the higher ones. Finally, the root-mean-square (rms) difference is slightly smaller for GSR (89, 183 ± 7 GHz) than for MWR, due to a reduced mean difference that is evident at very low PWV values. As discussed above, for LWP retrievals we do not have a reference to compare with. Therefore, the accuracy is estimated by the LWP fluctuations during clear-sky periods (i.e., zero liquid detected by the infrared radiometer). Note that the accuracy determined represents a minimum estimate of the LWP retrieval error. In fact, uncertainty in LWP retrievals results from a combination of the instrument noise, uncertainties in forward modeling (gas spectroscopy and liquid water dielectric constant), and the error intrinsic to the inverse method. When the accuracy is estimated by the LWP fluctuations during clear sky, the contribution of the uncertainties in the liquid water dielectric constant is not sufficiently represented; this likely results in an underestimation of the total retrieval error. The retrieval accuracies achieved during the experiment, in terms of rms difference with respect to radiosonde measurements for PWV and zero-liquid detection for LWP, are listed in Table IV. Values are well in agreement with the expectations based on simulations (Table III).

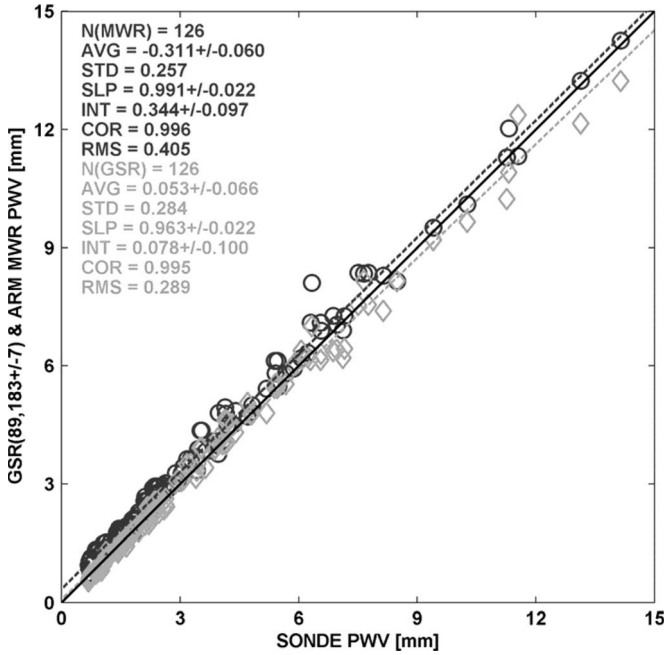

Fig. 13. Scatter plots of remotely sensed versus *in situ* PWV measurements. Circles indicate MWR PWV, whereas diamonds indicate GSR (89, 183.2 $\pm$ 7) PWV. Number of elements (N), mean X–Y difference (AVG), standard deviation (STD), slope (SLP), and intercept (INT) of linear fit, rms, and correlation coefficient (COR) are reported with corresponding colors. Uncertainties represent the 99% confidence interval.

TABLE IV
ACCURACY ACHIEVED WITH LINEAR REGRESSION APPLIED ON TWO-CHANNEL COMBINATIONS

CHANNEL COMBINATION	PWV (mm)	LWP (mm)
ARM MWR	0.41	0.0073
GSR(89,183±7)	0.28	0.0040

VI. SUMMARY, CONCLUSION, AND FUTURE WORK

Ground-based observations at cm, mm, and submm wavelengths were collected during the 2004 Arctic Winter Radiometric Experiment [4]. Measurements from three instruments are discussed in this paper: the ARM MWR (two channels), the ARM MWRP (12 channels), and the recently developed NOAA/PSD GSR (25 channels). The first two operate in the 22–31 GHz range (cm wave), whereas the last, at its first deployment, operates from 50–380 GHz (mm- and submm-wave). Using considerations about weighting functions and an analysis on both simulations and measurements, we demonstrated that mm- and submm-wavelengths offer enhanced sensitivity with respect to cm-wave radiometry to low amounts of PWV and LWP that are typical of the Arctic. A quantitative study of GSR channels' sensitivity was carried out, based on the experimental data, yielding enhancement factors from 1.5 to 69 for PWV and 3 to 4 for LWP when compared to 22–31-GHz channels.

However, the use of shorter wavelengths may involve significant scattering even within nonprecipitating clouds. As a consequence, special care is needed in the analysis of measurements showing a nonnegligible scattering contribution. Using the DOTLRT radiative transfer model [13], we evaluated the effect of hydrometeor scattering for the conditions that occurred during the experiment. We found that the scattering contribution remains within the instrumental noise for all but 340 and 380.20 $\pm$ 17 GHz channels. Therefore, radiative transfer based on pure emission may not be appropriate for modeling these channels during cloudy sky. This characteristic needs to be taken into account when including these channels in a retrieval scheme. Although it is beyond the scope of this paper, this feature also suggests that an opportune combination of GSR channels may offer the potential of retrieving IWP.

Due to the increased sensitivity we have demonstrated, mm- and submm-wavelength observations are expected to improve significantly the retrieval of PWV and LWP. Because of nonlinear behavior of some GSR channels, an appropriate nonlinear retrieval technique should be developed to exploit more fully the potential of this instrument. Nevertheless, using a simulated data set we demonstrated that in the dry conditions of the Arctic, a simple linear regression yields satisfactory results when applied on relatively transparent mm- and submm-wave channels. For a two-channel combination (e.g., 89 and 183 $\pm$ 7 GHz), the expected accuracy is on the order of 0.23 and 0.007 mm for PWV and LWP, respectively. Using conventional cm-wave channels (as 23.8 and 31.4 GHz), the expected accuracy is 0.37 mm for PWV and 0.012 mm for LWP.

An example of this linear regression applied to real observations is presented. Assuming the simultaneous measurements from radiosondes as a reference, we estimated the retrieval accuracy achieved for PWV. Since the radiosondes did not carry liquid water sensors, we rely on cloud detection from an infrared sensor to estimate the LWP accuracy during clear sky, although we recognize this represents just a minimum estimate of the LWP retrieval error. This analysis shows that retrievals based on GSR 89 and 183 $\pm$ 7 GHz channels lead to an accuracy of 0.28 mm for PWV and 0.004 mm for LWP; if MWR retrievals are used instead, the corresponding numbers are 0.41 and 0.007 mm for PWV and LWP, respectively. Thus, the accuracies determined experimentally are found in agreement with the theoretical expectations.

Finally, the use of nonlinear techniques would overcome the limitations imposed by the linear regression and exploit more fully the potential of GSR observations. Accordingly, a 1D-VAR is currently being implemented as part of our ongoing research.

APPENDIX
BASIC EQUATIONS

Introducing the cosmic background temperature T_c and the mean radiative temperature $T_{\rm mr}$ [7], we can express the downwelling radiance as

$$B_\nu(T_b) = B_\nu(T_c) \cdot e^{-\tau_\nu} + B_\nu(T_{\rm mr}) \cdot (1 - e^{-\tau_\nu}) \qquad \text{(A1)}$$

where B_ν is the Planck function computed at the frequency ν, and the atmospheric opacity τ (for simplicity, let us drop the frequency subscript) includes the contribution of dry air (τ_d),

water vapor (τ_V), and liquid water (τ_L). In clear sky, the liquid water contribution is null, and thus

$$\tau = \tau_d + \tau_V = \tau_d + \int_0^\infty \alpha_V(z)\rho(z)dz \tag{A2}$$

where α_V is the water vapor absorption coefficient. Assuming this varies only slightly with altitude, we introduce the average mass absorption coefficient k_V, such that

$$\tau = \tau_d + k_V V \tag{A3}$$

where with V we indicate the precipitable water vapor. In the case of low opacity ($\tau < 0.5$ Np), we can approximate (A1) as

$$B_\nu(T_b) = B_\nu(T_c) + \tau_d \cdot (B_\nu(T_{\rm mr}) - B_\nu(T_c)) + k_V \cdot (B_\nu(T_{\rm mr}) - B_\nu(T_c)) \cdot V. \tag{A4}$$

Expanding the Planck function in terms of $h\nu/kT$ (h and k are the Planck and Boltzmann constants, respectively) up to the second order, we can rewrite (A4) as

$$T_b = I + S \cdot V \tag{A5}$$

where

$$I \approx T_c + \tau_d(T_{\rm mr} - T_c) + (1 - \tau_d)\left(\frac{h\nu}{k}\right)^2 \frac{1}{12 \cdot T_c}$$

$$S \approx k_V(T_{\rm mr} - T_c) - \left(\frac{h\nu}{k}\right)^2 \frac{1}{12 \cdot T_c}.$$

REFERENCES

[1] J. A. Curry, W. B. Rossow, D. Randall, and J. L. Schramm, "Overview of Arctic cloud and radiation characteristics," *J. Clim.*, vol. 9, no. 8, pp. 1731–1764, Aug. 1996.

[2] P. E. Racette, E. R. Westwater, Y. Han, A. Gasiewski, M. Klein, D. Cimini, W. Manning, E. Kim, J. Wang, and P. Kiedron, "Measuring low amounts of precipitable water vapor using millimeter-wave radiometry," *J. Atmos. Ocean. Technol.*, vol. 22, no. 4, pp. 317–337, Apr. 2005.

[3] M. D. Shupe, T. Uttal, and S. Matrosov, "Arctic cloud microphysics retrievals from surface-based remote sensors at SHEBA," *J. Appl. Meteorol.*, vol. 44, no. 10, pp. 1544–1562, Oct. 2005.

[4] E. R. Westwater, D. Cimini, V. Mattioli, A. Gasiewski, M. Klein, V. Leuski, and J. Liljegren, "The 2004 North Slope of Alaska Arctic Winter Radiometric Experiment: Overview and highlights," in *Proc. Microw. Spec. Meeting*, San Juan, Puerto Rico, 2006, pp. 77–81.

[5] D. Cimini, E. R. Westwater, A. J. Gasiewski, M. Klein, V. Leusky, and S. Dowlatshahi, "The Ground-based Scanning Radiometer (GSR): A powerful tool for the study of the Arctic atmosphere," in *Proc. 15th ARM STM*, Daytona Beach, FL, 2005, pp. 1–14.

[6] M. Klein and A. J. Gasiewski, "Nadir sensitivity of passive millimeter and submillimeter wave channels to clear air temperature and water vapor variations," *J. Geophys. Res.*, vol. 105, no. D13, pp. 17 481–17 511, Jul. 2000.

[7] E. R. Westwater, "Ground-based microwave remote sensing of meteorological variables," in *Atmospheric Remote Sensing by Microwave Radiometry*, M. Janssen, Ed. Hoboken, NJ: Wiley, 1993, pp. 145–213.

[8] J. C. Lagarias, J. A. Reeds, M. H. Wright, and P. E. Wright, "Convergence properties of the Nelder–Mead simplex method in low dimensions," *SIAM J. Optim.*, vol. 9, no. 1, pp. 112–147, 1998.

[9] P. W. Rosenkranz, "Water vapor microwave continuum absorption: A comparison of measurements and models," *Radio Sci.*, vol. 33, no. 4, pp. 919–928, 1998.

[10] P. W. Rosenkranz, "Water vapor microwave continuum absorption: A comparison of measurements and models," *Radio Sci.*, vol. 34, no. 4, p. 1025, 1999.

[11] J. C. Liljegren, S. A. Boukabara, K. Cady-Pereira, and S. A. Clough, "The effect of the half-width of the 22-GHz water vapor line on retrievals of temperature and water vapor profiles with a 12-channel microwave radiometer," *IEEE Trans. Geosci. Remote Sens.*, vol. 43, no. 5, pp. 1102–1108, May 2005.

[12] J. A. Schroeder and E. R. Westwater, "Users' guide to WPL microwave radiative transfer software," NOAA Admin., Boulder, CO, Tech. Memo. ERL WPL-213, 1991.

[13] A. G. Voronovich, A. J. Gasiewski, and B. L. Weber, "A fast multistream scattering-based Jacobian for microwave radiance assimilation," *IEEE Trans. Geosci. Remote Sens.*, vol. 42, no. 8, pp. 1749–1761, Aug. 2004.

[14] G. M. Skofronick-Jackson, A. J. Gasiewski, and J. Wang, "Influence of microphysical cloud parameterizations on microwave brightness temperatures," *IEEE Trans. Geosci. Remote Sens.*, vol. 40, no. 1, pp. 187–196, Jan. 2002.

[15] M. P. Cadeddu, J. C. Liljegren, and A. Pazmany, "Measurements and retrievals from a new 183-GHz water-vapor radiometer in the Arctic," in *Proc. Microw. Spec. Meeting*, San Juan, Puerto Rico, 2006, pp. 252–255.

[16] C. D. Rodgers, *Inverse Methods for Atmospheric Sounding: Theory and Practice*. Singapore: World Scientific, 2000.

[17] D. Cimini, T. J. Hewison, L. Martin, J. Güldner, C. Gaffard, and F. S. Marzano, "Temperature and humidity profile retrievals from ground-based microwave radiometers during TUC," *Meteorol. Z.*, vol. 15, no. 1, pp. 45–56, Feb. 2006.

[18] T. J. Hewison and C. Gaffard, "1D-VAR retrieval of temperature and humidity profiles from ground-based microwave radiometers," in *Proc. Microrad*, San Juan, Puerto Rico, 2006, pp. 235–240.

[19] V. Mattioli, E. R. Westwater, D. Cimini, J. S. Liljegren, B. M. Lesht, S. I. Gutman, and F. J. Schmidlin, "Analysis of radiosonde and ground-based remotely sensed PWV data from the 2004 North Slope of Alaska Arctic Winter Radiometric Experiment," *J. Atmos. Ocean. Technol.*, vol. 24, no. 3, pp. 415–431, Mar. 2007.

Domenico Cimini was born in Teramo, Italy, in 1973. He received the Laurea degree in physics and the Ph.D. degree from the University of L'Aquila, L'Aquila, Italy, in 1998 and 2002, respectively.

In 1999, he collaborated with the Environmental Technology Laboratory, National Oceanic and Atmospheric Administration, Boulder, CO. In 2002, he joined the Center of Excellence (CETEMPS), University of L'Aquila, where he worked on radiometer calibration techniques, microwave radiative transfer models, and ground- and satellite-based passive microwave and infrared radiometry. During 2004-2005, he was a Visiting Fellow in the Cooperative Institute for Research in Environmental Sciences, University of Colorado, Boulder. Then, he joined the Institute of Methodologies for the Environmental Analysis (IMAA), Italian National Research Council (CNR), where he worked on ground- and satellite-based observations of cloud properties. Since 2006, he has been with the Center for Environmental Technology, Department of Electrical and Computer Engineering, University of Colorado, where he has been an Adjunct Professor since 2007. He is also currently with CETEMPS, University of L'Aquila.

Ed R. Westwater (SM'91–F'01) received the B.A. degree in physics and mathematics from the Western State College of Colorado, Gunnison, in 1959, the M.S. and Ph.D. degrees in physics from the University of Colorado, Boulder (CU) in 1962 and 1970, respectively.

From 1960 to 1995, he was with the U.S. Department of Commerce. Since 1995, he has been with the Cooperative Institute for Research in Environmental Science (CIRES), Department of Electrical and Computer Engineering (ECE), CU, and joined the U.S. National Oceanic and Atmospheric Administration-CU Center for Environmental Technology (CET), ECE, in 2006. He presented the American Meteorological Society's Remote Sensing Lecture in 1997. From 1999 to 2002, he served as an Associate Editor of *Radio Science*, and from 2000 to 2002, he was the Chairman of the International Union for Radio Science Commission F. He was the Chairman and Organizer of the 1992 International Specialists Meeting on Microwave Radiometry and Remote Sensing Applications (MicroRad) and was a Co-Organizer of MicroRad 2001. He is currently a Research Professor at CET and CIRES. He is the author or coauthor of more than 275 publications. His research interests are microwave absorption in the atmosphere, remote sensing of the atmosphere and ocean surface, microwave and infrared radiative transfer, ground- and satellite-based remote sensing by passive radiometry, and the application of mathematical inversion techniques to problems in remote sensing.

Dr. Westwater is a member of the American Meteorological Society, the American Geophysical Union, and the Mathematical Association of America. He received the 15th V. Vaisala Award from the World Meteorological Society in 2001 and the Distinguished Achievement Award from the IEEE Geoscience and Remote Sensing Society in 2003. He served as a Guest Editor of the IEEE TRANSACTIONS ON GEOSCIENCE AND REMOTE SENSING (TGARS) Special Issue devoted to MicroRad 2004 and of the TGARS Special Issue devoted to MicroRad 2006 and is currently an Associate Editor of TGARS.

Albin J. Gasiewski (SM'81–M'88–SM'95–F'02) received the B.S. degree in mathematics and the M.S. and B.S. degrees in electrical engineering from Case Western Reserve University, Cleveland, OH, in 1983 and the Ph.D. degree in electrical engineering and computer science from Massachusetts Institute of Technology, Cambridge, in 1989.

He is currently a Professor of electrical and computer engineering at the University of Colorado (CU), Boulder, and the Director of the Center for Environmental Technology, Department of Electrical and Computer Engineering, CU. From 1997 to 2005, he was with the Environmental Technology Laboratory (ETL), National Oceanic and Atmospheric Administration, Boulder, where he was Chief of the Microwave Systems Development Division, ETL. From 1989 to 1997, he was a Faculty Member in the School of Electrical and Computer Engineering, Georgia Institute of Technology, Atlanta, where he became an Associate Professor. He has developed and taught courses on electromagnetics, remote sensing, instrumentation, and wave propagation theory. His technical interests include passive and active remote sensing, radiative transfer, antennas and microwave circuits, electronic instrumentation, meteorology, and oceanography.

Prof. Gasiewski is a member of the American Meteorological Society, American Geophysical Union, International Union of Radio Scientists (URSI), Tau Beta Pi, and Sigma Xi. He is a recipient of the 2006 Outstanding Service Award from the Geoscience and Remote Sensing Society. He is a past President (2004–2005) of the IEEE Geoscience and Remote Sensing Society. He currently serves as a Vice Chair of United States National Committee URSI Commission F. He has served on the U.S. National Research Council's Committee on Radio Frequencies from 1989 to 1995. He was the General Cochair of the International Geoscience and Remote Sensing Symposium 2006 in Denver, CO.

Marian Klein (M'95) received the M.S. and Ph.D. degrees in electrical engineering from the Technical University of Košice (TU Košice), Košice, Slovak Republic, in 1996 and 1986, respectively.

From 1987 to 1996, he was a Faculty Member in the Faculty of Electrical Engineering and Informatics, TU Košice. From September 1996 to June 1997, he was a Fulbright Scholar in the Laboratory for Radio Science and Remote Sensing, Georgia Institute of Technology, Atlanta. Since August 1998, he has been a Research Associate in the Cooperative Institute for Research in Environmental Sciences, University of Colorado (CU), Boulder, and the Laboratory Manager in the Center for Environmental Technology (CET), CU. He is also the Chief Executive Officer of Boulder Environmental Sciences and Technology, LLC, Boulder. He has an extensive knowledge and experience in radiometer systems design for harsh environments—airborne or ground based. He successfully led many field deployments of radiometric systems used in many experiments of the National Aeronautics and Space Administration, National Oceanic and Atmospheric Administration (NOAA), Department of Energy, and Department of Defense, including several soil moisture experiments (1999, 2002, 2003, and 2004), the Wakasa Bay experiment (2003), the Cold Land Processes Experiments (2002 and 2003), and AMSR-E Arctic and Antarctic Sea Ice Experiments (2003 and 2004). He was a Project Leader for the ground-based scanning radiometer deployed in Barrow, AK (2004). He is a Lead Field Engineer and Design and Fabrication Leader for several NOAA/Environmental Technology Laboratory and CET instruments such as the Polarimetric Scanning Radiometer system including its PSR/A, PSR/CX and PSR/S scanheads. His areas of technical expertise include passive microwave remote sensing, radiative transfer theory, and the development of millimeter- and submillimeter-wave instrument systems for environmental studies.

Vladimir Ye Leuski received the M.S. degree in radio engineering from Moscow Aviation Institute, Moscow, Russia, in 1971 and Doctor's degree in radio physics from the Space Research Institute, Moscow, in 1984.

From 1974 to 1984, he was an Engineer and Senior Engineer at the Space Research Institute. From 1985 to 1990, he was with the Research Institute "Pulsar," Moscow, as the Chief of Laboratory. From 1991 to 1996, he was with the Lebedev Physical Institute, Moscow. Since July 1996, he has been a Research Associate in the Cooperative Institute for Research in Environmental Sciences, University of Colorado, Boulder. His main scientific interests are the developmental of low-noise millimeter-wave components and radiometers and their application for remote sensing of the atmosphere and ocean surface.

James C. Liljegren received the B.S., M.S., and Ph.D. degrees in mechanical engineering from the University of Illinois at Urbana-Champaign. His doctoral dissertation was on the development and field validation of a stochastic model of turbulent dispersion in the convective boundary layer.

In 1999, he joined Argonne National Laboratory, Argonne, IL, where he is currently an Atmospheric Scientist in the Decision and Information Sciences Division. He has been involved in the ARM Program since its inception in 1990 in Science Team and Infrastructure roles and has been the ARM Instrument Coordinator since 2003; he has participated in field campaigns at the ARM Southern Great Plains (SGP) and North Slope of Alaska sites that are focused on water vapor measurements, including an extended comparison of slant water measurements with GPS and microwave radiometers, and has served as the SGP Site Manager from 2000 to 2005; he also participated in the Surface Heat Budget of the Arctic campaign. His current research interests involve atmospheric remote sensing, primarily using passive microwave radiometry. His research efforts have included developing continuous autonomous calibration algorithms for ARM microwave radiometers, developing improved retrieval algorithms for precipitable water, cloud liquid water path, and vertical profiles of temperature and humidity, and refining the microwave spectroscopy underlying the retrievals.